HHS Public Access

Author manuscript

ACS Nano. Author manuscript; available in PMC 2016 June 04.

Published in final edited form as:

ACS Nano. 2016 January 26; 10(1): 1417–1424. doi:10.1021/acsnano.5b06860.

Pretargeted Positron Emission Tomography Imaging That Employs Supramolecular Nanoparticles with *in Vivo* Bioorthogonal Chemistry

Shuang Hou[†,‡,¶], **Jin-sil Choi**[‡,¶], **Mitch Andre Garcia**[‡,¶], **Yan Xing**[§], **Kuan-Ju Chen**[‡], **Yi-Ming Chen**[†], **Ziyue K. Jiang**[‡], **Tracy Ro**[‡], **Lily Wu**[‡], **David B. Stout**[‡], **James S. Tomlinson**[^], **Hao Wang**[⊥], **Kai Chen**[*,§], **Hsian-Rong Tseng**[*,‡], and **Wei-Yu Lin**[*,†]

[†]Department of Medicinal and Applied Chemistry, Kaohsiung Medical University, 100 Shih-Chuan 1st Road, Kaohsiung, 80708, Taiwan

[‡]Department of Molecular and Medical Pharmacology, California NanoSystems Institute (CNSI), University of California, Los Angeles, Los Angeles, California 90095-1770, United States

[§]Molecular Imaging Center, Department of Radiology, Keck School of Medicine, University of Southern California, Los Angeles, California 90033-9061, United States

[⊥]National Center for Nanoscience and Technology, 11 Beiyitiao Zhongguancun Haidian District, Beijing, 100190, People's Republic of China

[^]Department of Surgery, University of California, Los Angeles, Los Angeles, California 90095, United States

Abstract

A pretargeted oncologic positron emission tomography (PET) imaging that leverages the power of supramolecular nanoparticles with *in vivo* bioorthogonal chemistry was demonstrated for the clinically relevant problem of tumor imaging. The advantages of this approach are that (i) the pharmacokinetics (PKs) of tumor-targeting and imaging agents can be independently altered *via* chemical alteration to achieve the desired *in vivo* performance and (ii) the interplay between the two PKs and other controllable variables confers a second layer of control toward improved PET imaging. In brief, we utilized supramolecular chemistry to synthesize tumor-targeting nanoparticles containing transcyclooctene (TCO, a bioorthogonal reactive motif), called TCO⊂SNPs. After the intravenous injection and subsequent concentration of the TCO⊂SNPs in the tumors of living mice, a small molecule containing both the complementary bioorthogonal motif (tetrazine, Tz) and a positron-emitting radioisotope (^{64}Cu) was injected to react selectively

[*]**Corresponding Authors:** (K. Chen), ; Email: chenkai@med.usc.edu; (H.-R. Tseng), ; Email: hrtseng@mednet.ucla.edu; (W.-Y. Lin), ; Email: wylin@kmu.edu.tw

[¶]**Author Contributions**

S. Hou, J.-s. Choi, and M. A. Garica equally contributed to this work.

Supporting Information

The Supporting Information is available free of charge on the ACS Publications website at DOI: 10.1021/acsnano.5b06860. Synthesis and analysis of molecular building blocks (*i.e.,* Tz and TCO derivatives, Ad-PAMAM, and Ad-PEG), radiolabeling of Tz-DOTA, preparation of 64Cu-DHP⊂SNPs, and probe (*i.e.,* TCO⊂SNPs and ^{64}Cu-Tz) characterization (PDF)

Notes

The authors declare no competing financial interest.

and irreversibly to TCO. High-contrast PET imaging of the tumor mass was accomplished after the rapid clearance of the unreacted ^{64}Cu-Tz probe. Our nanoparticle approach encompasses a wider gamut of tumor types due to the use of EPR effects, which is a universal phenomenon for most solid tumors.

Graphical abstract

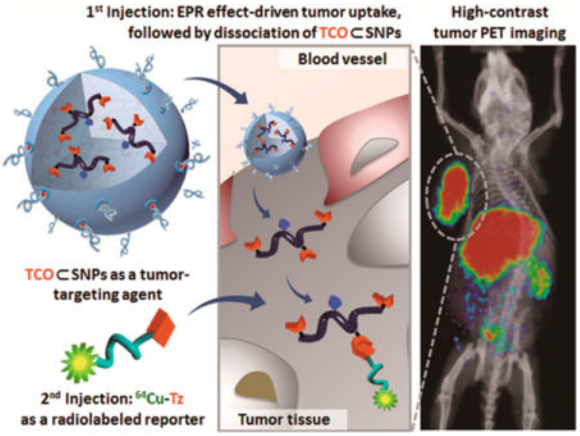

Keywords

supramolecular nanoparticles; bioorthogonal chemistry; PET imaging; pretargeted; EPR effect

Developing effective molecular imaging probes that can preferentially accumulate in tumors poses one of the major challenges in the field of oncologic imaging.[1–3] Over the years, researchers have exploited various molecular mechanisms that facilitate preferential uptake of probes in tumors while minimizing nonspecific retention elsewhere in the body. Using tumor positron emission tomography (PET) imaging[4–7] as an example, metabolic processes (*e.g.*, glycolysis) that are often amplified in tumor cells constitute the biochemical mechanisms driven by the development of small-molecule probes, *e.g.*, 2-deoxy-2-[^{18}F]fluoro-D-glucose.[8] Aside from small-molecule PET probes, affinity ligand-based probes, including peptides,[9–13] antibodies, and their engineered fragments,[14,15] are gaining importance as molecular imaging probes, which have been employed to selectively recognize subpopulations of tumor cells with overexpressed surface receptors. Alternatively, the enhanced permeability and retention (EPR) effect,[16,17] which facilitates accumulation of nanoparticle-based probes[18–23] in tumors, has also demonstrated its utility in tumor PET imaging under preclinical settings. However, these various approaches employed for the development of PET imaging probes are constrained by the intrinsic pharmacokinetics (PKs) of their underlying molecular mechanisms and limited half-lives ($T_{1/2}$) of positron-emitting radioisotopes, *e.g.*, ^{18}F ($T_{1/2}$ = 109.7 min), ^{64}Cu ($T_{1/2}$ = 12.7 h), and ^{124}I ($T_{1/2}$ = 4.17 d).[24] Since the tumor-targeting component and its radiolabeled reporter are often conjugated into a single agent in PET probes, the radiation signal may have significantly decayed by the time the probes achieve an optimal distribution in tumors. A promising solution to improve the performance of PET imaging probes may be capitalized by a pretargeted imaging strategy, which decouples the tumor-targeting agent from its radiolabeled reporter.

Pretargeted imaging[25–27] has been a well-established strategy used for several decades,[28–30] and numerous studies have demonstrated its success in improving both optical[31,32] and nuclear[33] imaging. Ideally, in a pretargeted PET imaging system, the tumor-targeting agent needs to be engineered with PKs that facilitate preferential accumulation in tumors within a reasonable time frame. In parallel, the respective radiolabeled reporter should be designed with a different PKs that enable effective whole-body distribution and rapid clearance. In order to achieve successful pretargeted imaging, the radiolabeled reporter needs to selectively and irreversibly couple to the tumor-targeting agent. Bioorthogonal conjugation chemistry[34–40] is an ideal solution due to its reaction specificity in living systems. In short, the advantages of pretargeted PET imaging strategy include (i) attenuating the PKs of both nanoparticles and radiolabeled imaging agents *via* rational molecular design to obtain optimal *in vivo* performances and (ii) modulating the interplay between the two PKs and other controllable variables (*e.g.*, injection times, radioisotopes, dosage) to confer a second layer of control toward improved PET imaging performance. For example, antibody-based pretargeted radioimaging, where antibodies were regarded as the tumor-targeting agent and radioisotopes (*i.e.*, ^{111}In, ^{64}Cu, and 18F),[41–44] was incorporated into the corresponding radiolabeled reporters. Although applying an engineered antibody in conjunction with the pretargeted imaging strategy was able to achieve good tumor imaging performance, such an approach might be limited for detecting subpopulations of cancer cells with an overexpressed surface marker; thus, developing new imaging probes capable of targeting universal tumor phenotypes (*e.g.*, leaky tumor vascular structures that lead to the tumor EPR effect) could offer an alternative solution. The feasibility of nanoparticle-based pretargeted tumor imaging has been demonstrated using mesoporous silica nanoparticles[45] in conjunction with a bioorthogonal chemistry based on strain-promoted alkyne azide cycloaddition (k_2 = 0.01–1 $M^{-1}{\cdot}s^{-1}$).[46] It is conceivable that by replacing the alkyne–azide bioorthogonal reaction with a more reactive one based on inverse electron-demand Diels–Alder reaction ($k_2 \approx 10^4$ $M^{-1}{\cdot}s^{-1}$)[39,46] an improved pretargeted imaging performance can be achieved.

Herein, we introduce a new approach (Figure 1) for pretargeted oncologic PET imaging that leverages the power of *in vivo* bioorthogonal chemistry and a supramolecular nanoparticle (SNP) vector pioneered by our research group.[47] In this approach, a reactive bioorthogonal motif (*trans*-cyclooctene, TCO; inverse electron-demand Diels–Alder reaction, $k_2 \approx 10^4$ $M^{-1}{\cdot}s^{-1}$)[39,46] is encapsulated into an SNP vector to provide TCO⊂SNPs with a uniform size of ca. 100 nm (Figure 1a). TCO⊂SNPs can then serve as a tumor-targeting agent that promises preferential accumulation in tumors as a consequence of the EPR effects (Figure 1b). The supramolecular synthetic strategy confers a dynamic nature[47,48] to the self-assembled TCO⊂SNPs. After TCO⊂SNPs are accumulated in tumor, tumor-retained TCO⊂SNPs can disassemble to release a TCO-grafted molecular building block, TCO-grafted cyclodextrin-polyethylenimine polymer (TCO/CD-PEI, Supporting Information Section 1; Figure 1c), for bioorthogonal ligation with a complementary bioorthogonal motif (*i.e.*, a tetrazine group, Tz) on the subsequently injected radiolabeled reporter (^{64}Cu-Tz, Supporting Information Sections 2 and 3; Figure 1d). The resulting dihydropyrazine (DHP) conjugation adduct 64Cu-DHP/CD-PEI confines radioactivity in the tumor, resulting in

high-contrast tumor PET imaging after rapid clearance of free ^{64}Cu-Tz from the animal (Figure 1e–g).

RESULTS AND DISCUSSION

The supramolecular strategy is capable of accurately controlling the sizes, surface chemistry, zeta potentials, and payloads of the SNP-based vectors and has demonstrated its powerful utility in a wide range of biomedical applications, e.g., PET imaging,[47,49] magnetic resonance imaging (MRI),[50] photothermal treatment of cancer cells,[51] and highly efficient delivery of genes,[48,52–55] proteins,[55] and drugs.[49,56] We then employed a supramolecular synthetic strategy[47] (Figure 2a) to prepare the tumor-targeting agent, 100 nm TCO⊂SNPs, *via* self-assembly from four molecular building blocks, *i.e.*, TCO/CD-PEI, CD-PEI,[47] adamantane-grafted polyamidoamine (Ad-PAMAM),[47] and Ad-grafted polyethylene glycol (Ad-PEG).[47] We note that the TCO-grafted molecular building block TCO/CD-PEI was prepared from an existing compound, CD-PEI (Figure S2 in the Supporting Information).[47] By fine-tuning the mixing ratios among the four molecular building blocks, the sizes and surface chemistry that affect the PKs of TCO⊂SNPs can be precisely controlled.[47–49,52] Transmission electron microscope (TEM) images (Figures 2b and S5) and dynamic light scattering (DLS) measurements (Figure 2c) show a spherical morphology and narrow size distribution for 100 nm TCO⊂SNPs (hydrodynamic size (DLS): 100 ± 20 nm, TEM: 90.9 ± 8.6 nm). Encapsulating the bioorthogonal TCO groups inside the nanoparticular spaces of TCO⊂SNPs offers three advantages: (i) overcoming the low water solubility of the hydrophobic TCO motif, (ii) enhancing the loading capacity of TCO motifs, and (iii) protecting the reactive TCO motifs from potential degradation over the course of delivery. As a result, the overall delivery efficiency of TCO motifs can be improved. In parallel, the radiolabeled reporter ^{64}Cu-Tz can be prepared by a one-step radiometal labeling procedure from the respective precursor (tetrazine-DOTA; Supporting Information Section 3). After the EPR-driven accumulation of TCO⊂SNPs in a tumor, the tumor-retained TCO⊂SNPs can dynamically disassemble to release TCO/CD-PEI (Figure 1c).[47,48] Subsequently, the ^{64}Cu-Tz is injected for bioorthogonal reaction with TCO/CD-PEI *in vivo*, yielding the dihydropyrazine conjugation adduct, 64Cu-DHP/CD-PEI. Therefore, radioactivity is locally confined to the tumor and can be visualized and semiquantified with PET imaging technology.

For pretargeted studies, sterilized TCO⊂SNPs (100 μg, equivalent to 1 nmol of TCO, 1 μg/μL) were injected into mice *via* the tail vein. Xenografted mouse models were prepared by subcutaneously injecting U87 glioblastoma cells (2×10^6 cells) into the right shoulder of nude mice (Nu/Nu, $n = 4$). MicroPET imaging studies (Figure 3) were carried out when the tumors grew to 7 mm × 7 mm. After 24 h of TCO⊂SNPs distribution at the tumor site, freshly prepared and purified ^{64}Cu-Tz (300 μCi of ^{64}Cu, 100 μL, equivalent to 10 nmol of Tz) in saline was then injected *via* tail vein (Figure 3a). At various time points the anesthetized animals ($n = 4$) were positioned on the PET scanner bed, and a static PET scan was acquired for 10 min. As illustrated in Figure 3b, a strong PET signal was observed at the tumor site, indicating efficient formation of ^{64}Cu-DHP/CD-PEI. The highest tumor to liver signal ratio appears at 24 h postinjection (p.i.), suggesting that nanoparticles were retained in tumor through the EPR effect (Figure 3c).

To demonstrate the superiority of the pretargeted strategy, sequential injection of TCO⊂SNPs (100 μg) and ^{64}Cu-Tz (300 μCi of ^{64}Cu), we carried out two *in vivo* control studies, namely, (i) injection of the free radiolabeled reporter (^{64}Cu-Tz) alone without any nanoparticles and (ii) SNP control, in which ^{64}Cu-Tz reacted with TCO⊂SNPs first to form ^{64}Cu-DHP⊂SNPs prior to injection and subsequent imaging of the ^{64}Cu-DHP⊂SNPs product. Figure 4 details the experimental timeline implemented for the pretargeted imaging strategy and the two control studies, *i.e.*, free radiolabeled reporter (^{64}Cu-Tz) and SNP control (^{64}Cu-DHP⊂SNPs); the imaging time point, 24 h p.i. of ^{64}Cu-Tz, was determined from a preliminary pretargeted study (Figure 3). The mice (n = 4) were first placed into a microPET scanner (Focus 220, Siemens Preclinical Solutions, Knoxville, TN, USA), immediately followed by an X-ray computed tomography (CT) scanner (MicroCAT II, Siemens Preclinical Solutions, Knoxville, TN, USA) to acquire combination PET/CT images. Mice were kept warm at all times, immobilized using 1–2% isoflurane inhalent anesthesia, and positioned using a common imaging chamber for both systems. PET images were obtained at ~1.8 mm resolution using filtered back projection, and CT images were acquired with 0.2 mm voxels for a resolution of ~0.4 mm. Representative microPET/CT fused images of xenografted mice in the pretargeted, SNP control, and free radiolabeled reporter (^{64}Cu-Tz) studies are shown in Figure 4a–c. In the case of the pretargeted studies, the accumulation and retention of radioactivity occurred mainly in the tumor and liver with some nonspecific uptake in normal tissues, thereby demonstrating improved tumor-imaging performance in contrast to that obtained by the SNP control studies. We note that the high radioactivity observed in the liver for all three studies partially reflects the well-known demetalation (*i.e.*, dissociation of $^{64}Cu^{2+}$ from the DOTA ligand; Supporting Information, Figure S5) of the $^{64}Cu^{2+}$-labeled reporter (^{64}Cu-Tz).[57] Presumably, this issue can be overcome by using a radioisotope (*e.g.*, 18F) that is covalently attached to the radiolabeled reporter.

After PET/CT scanning (24 h p.i. of PET probes), mice were euthanized and their major organs and tumors were excised to provide quantitative *ex vivo* biodistribution of the PET probe. The organs and tumors were weighed, and radioactivity was counted by a gamma counter (PerkinElmer, Waltham, MA, USA) to determine the percent injected dose per each gram of organ tissue (% ID/g). As shown in Figure 5, the tumor/liver radioactivity uptakes in all three studies were 16/17 (pretargeted; the value is consistent with the tumor to liver signal ratio shown in Figure 3c), 3.5/24 (SNP control), and 1.6/3.7 (radiolabeled reporter) percent injected dose per gram of tissue (% ID/g) at 24 h p.i. The radioactivity in blood stayed approximately the same in both the pretargeted study (2.6%) and the SNP control (2.7%), whereas the radioactivity in blood for the free probe ^{64}Cu-Tz was much lower (1.6% ID/g) due to its quick clearance out of the body (Supporting Information, Figure S7 and S8). The pretargeted study had the highest percent injected dose in the tumor, indicating the occurrence of a bioorthogonal ligation reaction between TCO/CD-PEI and ^{64}Cu-Tz as a result of confinement of ^{64}Cu-DHP/CD-PEI in the tumor. In addition, the tumor to blood ratio for the pretargeted study is over 3-fold higher than that for the SNP control and the free radiolabeled reporter (Figure 5b), quantitatively confirming that the observed improvement in imaging quality can be achieved by our pretargeted PET imaging approach.

CONCLUSION

We have demonstrated a new pretargeted imaging approach that leverages the power of supramolecular nanoparticles and *in vivo* bioorthogonal chemistry to achieve superb preclinical oncologic PET imaging. In contrast to conventional imaging approaches, the pretargeted strategy decouples a tumor-targeting agent (*i.e.*, TCO⊂SNPs) from a radiolabeled imaging agent (^{64}Cu-Tz). Compared to previous pretargeted approaches based on monoclonal antibodies, our nanoparticle approach encompasses a wider gamut of tumor types due to the use of the EPR effect, which is a common phenomenon in most solid tumors. As opposed to traditional nanoparticle-based imaging platforms, which usually end up with high liver uptake but weak tumor uptake, our approach already shows approximately equivalent uptake in both tumor and liver. We hope that our pretargeted approach will change the current paradigm in oncologic imaging, providing a robust improved methodology for researchers and clinicians to pursue.

MATERIALS AND METHODS

Materials

Reagents and solvents were purchased from Sigma-Aldrich (St. Louis, MO, USA) and used as received unless otherwise noted. 1-Admantanamine hydrochloride and β-cyclodextrin were purchased from TCI America (San Francisco, CA, USA). First-generation polyamidoamine dendrimer with 1,4-diaminobutane core and amine terminals in 20% by weight methanol solution was purchased from Dendritic Nanotechnologies, Inc. (Mount Pleasant, MI, USA). N-Hydroxysuccinimide (NHS)-functionalized methoxyl polyethylene glycol (mPEG-NHS, MW = 5 kDa) was obtained from NANOCS Inc. (New York, NY, USA). CD-grafted branched polyethylenimine (CD-PEI), CD-grafted transcyclooctene polyethylenimine (TCO/CD-PEI), Ad-grafted PAMAM (Ad-PAMAM), and Ad-grafted polyethylene glycol (Ad-PEG) were prepared *via* the method previously reported by our group.[47] Phosphate-buffered saline (PBS) was obtained from Invitrogen (Carlsbad, CA, USA).

Synthesis of TCO/CD-PEI

To a solution of CD-PEI (1.6 mg, 0.1 μmol, 1.0 equiv) in $NaHCO_3$ buffer solution (pH 8.4) was added TCO-NHS 9 (0.35 mg, 1.0 μmol, 10.0 equiv) in DMF (100 μL), and the reaction mixture was stirred at room temperature for 6 h. After the reaction was complete, the mixture was purified by dialysis (Slide-A-Lyzer dialysis cassette, MWCO 10 kDa) against DI water overnight and lyophilized to yield TCO/CD-PEI. More synthetic details and structural analysis (NMR and MS) are described in Supporting Information Section 1.

Preparation of ^{64}Cu-Tz

All liquids were pretreated with Chelex-100 (Bio-Rad, Hercules, CA, USA) to remove trace metal contaminants. The positron-emitting isotope ^{64}Cu (copper chloride in 0.1 mol/L HCl; radionuclide purity, >99%) was provided by Mallinckrodt Institute of Radiology (Washington University School of Medicine, St. Louis, WA, USA). The DOTA-conjugated tetrazine was dissolved (1 mg/mL) in 0.2 M ammonium acetate pH 6.0 and stored at −80 °C

before use. An aliquot of DOTA-conjugated tetrazine was combined with a suitable amount of [^{64}Cu]copper chloride and incubated for 10 min at 50 °C. Then, 5 μL of 10 mM DTPA was added, and the solution was incubated for additional 5 min. Radiochemical purities greater than 98% were obtained using this method, as confirmed by radio-HPLC (Figure S4). The specific activity of ^{64}Cu-Tz was estimated to be 300 mCi/μmol.

Preparation of TCO⊂SNPs

To a solution of Ad-PEG (150 μg) in 150 μL of PBS buffer was slowly injected Ad-PAMAM (5 μg) in 10 μL of DMSO *via* a Hamilton syringe under vigorous stirring. A 100 μL amount of PBS buffer containing CD-PEI (50 μg) and TCO-CD-PEI (50 μg) was sequentially added into the mixture to obtain TCO⊂SNPs.

Characterization Methods of TCO⊂SNPs

Dynamic Light Scattering—DLS experiments were performed with a Zetasizer Nano instrument (Malvern Instruments Ltd., United Kingdom) equipped with a 10 mW helium–neon laser (λ = 632.8 nm) and a thermoelectric temperature controller. Measurements were taken at a 90° scattering angle. The hydrodynamic size of the TCO⊂SNPs was measured by using DLS. The sizes were obtained by averaging the values of three measurements.

Transmission Electron Microscopy—The morphology and sizes of TCO⊂SNPs were examined using a transmission electron microscope. The studies were carried out on a Philips CM 120 electron microscope, operating at an acceleration voltage of 120 kV. The TEM samples were prepared by drop-coating 2 μL of sample suspension solutions onto carbon-coated copper grids. Excess amounts of solution were removed by filter papers after 45 s. Subsequently, the samples were negatively stained with 2% uranyl acetate for 45 s before TEM studies. Sizes were determined by averaging the measured value from 100 single TCO⊂SNPs in TEM images.

In Vivo microPET/CT Imaging

Mice were purchased from Jackson Laboratory (Bar Harbor, ME, USA). All animal manipulations were performed with sterile techniques and were approved by the University of California at Los Angeles Animal Research Committee. Xenografted mouse models were prepared by subcutaneously injecting U87 glioblastoma cells (2×10^6 cells) into the right shoulder of nude mice (Nu/Nu). Micro-PET/CT imaging studies were carried out when the tumors grew to 7 mm × 7 mm (n = 4/group).

MicroPET imaging was performed with a microPET FOCUS 220 PET scanner (Siemens Preclinical Solutions, Knoxville, TN, USA). All mice were anesthetized 15 min prior to imaging by using 1.5–2% isoflurane in a heated (30 °C) induction chamber and then transferred to a heated isolation/imaging chamber. PET images were reconstructed by filtered back projection. Results indicated that the highest tumor/liver PET signal occurred at 24 h postinjection.

Immediately after the microPET scan, mice underwent a 10 min MicroCAT II CT scan (Siemens) using routine image acquisition parameters. The microCT scan was used for

anatomical localization of the tissue concentrations of the ^{64}Cu over time by microPET. After scanning, tumors and major organs were excised, weighed, and counted in a gamma counter (Cobra II AutoGamma, Packard, IL, USA).

Pretargeted Study (^{64}Cu-Tz/TCO⊂SNPs)

Sterilized TCO⊂SNPs (100 μg, equivalent to 1 nmol of TCO, 1 μg/μL) were injected into the mice (n = 4) via the tail vein; the volume used for the tail vein injections was ~150 μL. After 24 h, freshly prepared and purified ^{64}Cu-Tz (300 μCi of ^{64}Cu, 100 μL, equivalent to 10 nmol of Tz) in saline was then injected *via* tail vein. Combined micro-PET/CT images were taken at various times p.i. of ^{64}Cu-Tz (Figures 3 and 4a).

SNP Control Study (^{64}Cu-DHP⊂SNPs)

The ^{64}Cu-DHP⊂SNPs were prepared as described in the Supporting Information. The sterilized adduct, ^{64}Cu-DHP⊂SNPs (100 μg, 1 μg/μL), was injected into the mice *via* the tail vein; the volume used for the tail vein injections was ~150 μL. Combined micro-PET/CT images were taken at 24 h p.i. of ^{64}Cu-DHP⊂SNPs (Figure 4b).

Free Radiolabeled Reporter Study (^{64}Cu-Tz)

Freshly prepared and purified ^{64}Cu-Tz (300 μCi of ^{64}Cu, 100 μL, equivalent to 10 nmol of Tz) in saline was systemically injected *via* tail vein. Combined micro-PET/CT images were taken at 24 h p.i. of ^{64}Cu-Tz (Figure 4c).

Ex Vivo Studies

At the termination time point of PET imaging studies, major organs were weighed and radioactivity was counted by a gamma counter (PerkinElmer, Waltham, MA, USA) to determine the percent injected dose per each gram of organ tissue. The *ex vivo* biodistribution data comparing the quantified radioactivity in various organs for each study are summarized in Figure 5. Data are presented as mean ± standard deviation (n = 4).

Supplementary Material

Refer to Web version on PubMed Central for supplementary material.

Acknowledgments

This research was supported by the Ministry of Science and Technology, Taiwan (NSC 102-2113-M-037-018-MY2 and MOST 103-2632-M-037-001), National Institutes of Health (R21GM098982 and R21EB016270), Donald E. and Delia B. Baxter Foundation, and National Science Council of the Republic of China. W.Y.L. thanks KMU for financial support. M.A.G. thanks the NIH for a postdoctoral fellowship through the Scholars in Oncologic Molecular Imaging (SOMI) program at UCLA. We are especially grateful to Waldemar Ladno at the Crump Institute for Molecular Imaging at UCLA for his assistance with the small-animal PET/CT scans.

References

1. Silverman DH, Cummings JL, Small GW, Gambhir SS, Chen W, Czernin J, Phelps ME. Added Clinical Benefit of Incorporating 2-Deoxy-2-[^{18}F]Fluoro-D-Glucose with Positron Emission Tomography into the Clinical Evaluation of Patients with Cognitive Impairment. Mol Imag Biol. 2002; 4:283–293.

2. Weissleder R, Pittet MJ. Imaging in the Era of Molecular Oncology. Nature. 2008; 452:580–589. [PubMed: 18385732]
3. Waldman AD, Jackson A, Price SJ, Clark CA, Booth TC, Auer DP, Tofts PS, Collins DJ, Leach MO, Rees JH. Quantitative Imaging Biomarkers in Neuro-Oncology. Nat Rev Clin Oncol. 2009; 6:445–454. [PubMed: 19546864]
4. Phelps ME, Hoffman EJ, Huang SC, Kuhl DE. Ecat: A New Computerized Tomographic Imaging System for Positron-Emitting Radiopharmaceuticals. J Nucl Med. 1978; 19:635–647. [PubMed: 660276]
5. Phelps ME. Positron Emission Tomography Provides Molecular Imaging of Biological Processes. Proc Natl Acad Sci U S A. 2000; 97:9226–9233. [PubMed: 10922074]
6. Czernin J, Phelps ME. Positron Emission Tomography Scanning: Current and Future Applications. Annu Rev Med. 2002; 53:89–112. [PubMed: 11818465]
7. Phelps, ME. PET: Molecular Imaging and Its Biological Applications. Springer; New York: 2004.
8. Ido T, Wan CN, Casella V, Fowler JS, Wolf AP, Reivich M, Kuhl DE. Labeled 2-Deoxy-D-Glucose Analogs-F-18-Labeled 2-Deoxy-2-Fluoro-D-Glucose, 2-Deoxy-2-Fluoro-D-Mannose and C-14–2-Deoxy-2-Fluoro-D-Glucose. J Labelled Compd Radiopharm. 1978; 14:175–183.
9. Gagnon MK, Hausner SH, Marik J, Abbey CK, Marshall JF, Sutcliffe JL. High-Throughput *in Vivo* Screening of Targeted Molecular Imaging Agents. Proc Natl Acad Sci U S A. 2009; 106:17904–17909. [PubMed: 19815497]
10. Tweedle MF. Peptide-Targeted Diagnostics and Radio-therapeutics. Acc Chem Res. 2009; 42:958–968. [PubMed: 19552403]
11. Chen K, Conti PS. Target-Specific Delivery of Peptide-Based Probes for Pet Imaging. Adv Drug Delivery Rev. 2010; 62:1005–1022.
12. Lee S, Xie J, Chen X. Peptides and Peptide Hormones for Molecular Imaging and Disease Diagnosis. Chem Rev. 2010; 110:3087–3111. [PubMed: 20225899]
13. Quan Q, Yang M, Gao H, Zhu L, Lin X, Guo N, Zhang G, Eden HS, Niu G, Che X. Imaging Tumor Endothelial Marker 8 Using an ^{18}F-Labeled Peptide. Eur J Nucl Med Mol Imaging. 2011; 38:1806–1815. [PubMed: 21814853]
14. Wu AM, Senter PD. Arming Antibodies: Prospects and Challenges for Immunoconjugates. Nat Biotechnol. 2005; 23:1137–1146. [PubMed: 16151407]
15. Wu AM. Antibodies and Antimatter: The Resurgence of Immuno-PET. J Nucl Med. 2009; 50:2–5. [PubMed: 19091888]
16. Matsumura Y, Maeda H. A New Concept for Macromolecular Therapeutics in Cancer Chemotherapy: Mechanism of Tumoritropic Accumulation of Proteins and the Antitumor Agent Smancs. Cancer Res. 1986; 46:6387–6392. [PubMed: 2946403]
17. Davis ME, Chen ZG, Shin DM. Nanoparticle Therapeutics: An Emerging Treatment Modality for Cancer. Nat Rev Drug Discovery. 2008; 7:771–782. [PubMed: 18758474]
18. Cheon J, Lee JH. Synergistically Integrated Nanoparticles as Multimodal Probes for Nanobiotechnology. Acc Chem Res. 2008; 41:1630–1640. [PubMed: 18698851]
19. Choi JS, Park JC, Nah H, Woo S, Oh J, Kim KM, Cheon GJ, Chang Y, Yoo J, Cheon J. A Hybrid Nanoparticle Probe for Dual-Modality Positron Emission Tomography and Magnetic Resonance Imaging. Angew Chem, Int Ed. 2008; 47:6259–6262.
20. Welch MJ, Hawker CJ, Wooley KL. The Advantages of Nanoparticles for PET. J Nucl Med. 2009; 50:1743–1746. [PubMed: 19837751]
21. Davis ME, Schluep T, Hwang J, Hildebrandt IJ, Czernin J, Choi CHJ, Alabi CA, Mack BC. Pharmacokinetics and Tumor Dynamics of the Nanoparticle It-101 from Pet Imaging and Tumor Histological Measurements. Proc Natl Acad Sci U S A. 2009; 106:11394–11399. [PubMed: 19564622]
22. Tang L, Yang X, Dobrucki LW, Chaudhury I, Yin Q, Yao C, Lezmi S, Helferich WG, Fan TM, Cheng J. Aptamer-Functionalized, Ultra-Small, Monodisperse Silica Nanoconjugate for Targeted Dual-Modal Imaging of Lymph Nodes with Metastatic Tumors. Angew Chem. 2012; 51:12721–12726. [PubMed: 23136130]
23. Qiao Z, Shi X. Dendrimer-Based Molecular Imaging Contrast Agents. Prog Polym Sci. 2015; 44:1–27.

24. Ametamey SM, Honer M, Schubiger PA. Molecular Imaging with PET. Chem Rev. 2008; 108:1501–1516. [PubMed: 18426240]
25. Goldenberg DM, Sharkey RM. Novel Radiolabeled Antibody Conjugates. Oncogene. 2007; 26:3734–3744. [PubMed: 17530026]
26. Goldenberg DM, Chatal JF, Barbet J, Boerman O, Sharkey RM. Cancer Imaging and Therapy with Bispecific Antibody Pretargeting. Update Cancer Ther. 2007; 2:19–31. [PubMed: 18311322]
27. van Duijnhoven SMJ, Rossin R, van den Bosch SM, Wheatcroft MP, Hudson PJ, Robillard MS. Diabody Pretargeting with Click Chemistry *in Vivo*. J Nucl Med. 2015; 56:1422–1428. [PubMed: 26159589]
28. Goodwin D, Meares C, Diamanti C, Mccall M, Lai C, Torti F, Mctigue M, Martin B. Use of Specific Antibody for Rapid Clearance of Circulating Blood Background from Radiolabeled Tumor Imaging Proteins. Eur J Nucl Med. 1984; 9:209–215. [PubMed: 6428891]
29. Goodwin DA, Meares CF, David GS, Mctigue M, Mccall MJ, Frincke JH, Stone MR, Bartholomew RA, Leung JP. Monoclonal-Antibodies as Reversible Equilibrium Carriers of Radiopharmaceuticals. Clin Nucl Med. 1985; 10:P10–P10.
30. Goodwin DA, Meares CF, David GF, Mctigue M, Mccall MJ, Frincke JM, Stone MR, Bartholomew RM, Leung JP. Monoclonal-Antibodies as Reversible Equilibrium Carriers of Radiopharmaceuticals. Nucl Med Biol. 1986; 13:383–391.
31. Perrault SD, Chan WC. *In Vivo* Assembly of Nanoparticle Components to Improve Targeted Cancer Imaging. Proc Natl Acad Sci U S A. 2010; 107:11194–11199. [PubMed: 20534561]
32. Agasti SS, Liong M, Tassa C, Chung HJ, Shaw SY, Lee H, Weissleder R. Supramolecular Host-Guest Interaction for Labeling and Detection of Cellular Biomarkers. Angew Chem, Int Ed. 2012; 51:450–454.
33. Kraeber-Bodere F, Salaun PY, Oudoux A, Goldenberg DM, Chatal JF, Barbet J. Pretargeted Radioimmunotherapy in Rapidly Progressing, Metastatic, Medullary Thyroid Cancer. Cancer. 2010; 116:1118–1125. [PubMed: 20127952]
34. Sletten EM, Bertozzi CR. From Mechanism to Mouse: A Tale of Two Bioorthogonal Reactions. Acc Chem Res. 2011; 44:666–676. [PubMed: 21838330]
35. Devaraj NK, Weissleder R. Biomedical Applications of Tetrazine Cycloadditions. Acc Chem Res. 2011; 44:816–827. [PubMed: 21627112]
36. Bertozzi CR, Sletten EM. Bioorthogonal Chemistry: Fishing for Selectivity in a Sea of Functionality. Angew Chem, Int Ed. 2009; 48:6974–6998.
37. Lim RK, Lin Q. Bioorthogonal Chemistry: Recent Progress and Future Directions. Chem Commun. 2010; 46:1589–1600.
38. Haun JB, Devaraj NK, Hilderbrand SA, Lee H, Weissleder R. Bioorthogonal Chemistry Amplifies Nanoparticle Binding and Enhances the Sensitivity of Cell Detection. Nat Nanotechnol. 2010; 5:660–665. [PubMed: 20676091]
39. Karver MR, Weissleder R, Hilderbrand SA. Synthesis and Evaluation of a Series of 1,2,4,5-Tetrazines for Bioorthogonal Conjugation. Bioconjugate Chem. 2011; 22:2263–2270.
40. Zeng D, Zeglis BM, Lewis JS, Anderson CJ. The Growing Impact of Bioorthogonal Click Chemistry on the Development of Radiopharmaceuticals. J Nucl Med. 2013; 54:829–832. [PubMed: 23616581]
41. Robillard MS, Rossin R, Verkerk PR, van den Bosch SM, Vulders RCM, Verel I, Lub J. *In Vivo* Chemistry for Pretargeted Tumor Imaging in Live Mice. Angew Chem, Int Ed. 2010; 49:3375–3378.
42. Devaraj NK, Thurber GM, Keliher EJ, Marinelli B, Weissleder R. Reactive Polymer Enables Efficient *in Vivo* Bioorthogonal Chemistry. Proc Natl Acad Sci U S A. 2012; 109:4762–4767. [PubMed: 22411831]
43. Emmetiere F, Irwin C, Viola-Villegas NT, Longo V, Cheal SM, Zanzonico P, Pillarsetty N, Weber WA, Lewis JS, Reiner T. ^{18}F–Labeled-Bioorthogonal Liposomes for *in Vivo* Targeting. Bioconjugate Chem. 2013; 24:1784–1789.
44. Zeglis BM, Sevak KK, Reiner T, Mohindra P, Carlin SD, Zanzonico P, Weissleder R, Lewis JS. A Pretargeted Pet Imaging Strategy Based on Bioorthogonal Diels–Alder Click Chemistry. J Nucl Med. 2013; 54:1389–1396. [PubMed: 23708196]

45. Lee SB, Kim HL, Jeong H-J, Lim ST, Sohn M-H, Kim DW. Mesoporous Silica Nanoparticle Pretargeting for PET Imaging Based on a Rapid Bioorthogonal Reaction in a Living Body. Angew Chem, Int Ed. 2013; 52:10549–10552.

46. Rahim MK, Kota R, Lee S, Haun JB. Bioorthogonal Chemistries for Nanomaterial Conjugation and Targeting. Nanotechnol Rev. 2013; 2:215–227.

47. Wang H, Wang S, Su H, Chen KJ, Armijo AL, Lin WY, Wang Y, Sun J, Kamei K, Czernin J, Radu CG, Tseng HR. A Supramolecular Approach for Preparation of Size-Controlled Nanoparticles. Angew Chem, Int Ed. 2009; 48:4344–4348.

48. Wang H, Liu K, Chen KJ, Lu Y, Wang S, Lin WY, Guo F, Kamei K, Chen YC, Ohashi M, Wang M, Garcia MA, Zhao XZ, Shen CK, Tseng HR. A Rapid Pathway toward a Superb Gene Delivery System: Programming Structural and Functional Diversity into a Supramolecular Nanoparticle Library. ACS Nano. 2010; 4:6235–6243. [PubMed: 20925389]

49. Lee J-H, Chen K-J, Noh S-H, Garcia MA, Wang H, Lin W-Y, Jeong H, Kong BJ, Stout DB, Cheon J, Tseng H-R. On-Demand Drug Release System for *in Vivo* Cancer Treatment through Self-Assembled Magnetic Nanoparticles. Angew Chem, Int Ed. 2013; 52:4384–4388.

50. Chen KJ, Wolahan SM, Wang H, Hsu CH, Chang HW, Durazo A, Hwang LP, Garcia MA, Jiang ZK, Wu L, Lin YY, Tseng HR. A Small MRI Contrast Agent Library of Gadolinium(III)-Encapsulated Supramolecular Nanoparticles for Improved Relaxivity and Sensitivity. Biomaterials. 2011; 32:2160–2165. [PubMed: 21167594]

51. Wang S, Chen KJ, Wu TH, Wang H, Lin WY, Ohashi M, Chiou PY, Tseng HR. Photothermal Effects of Supramolecularly Assembled Gold Nanoparticles for the Targeted Treatment of Cancer Cells. Angew Chem, Int Ed. 2010; 49:3777–3781.

52. Wang H, Chen KJ, Wang S, Ohashi M, Kamei K, Sun J, Ha JH, Liu K, Tseng HR. A Small Library of DNA-Encapsulated Supramolecular Nanoparticles for Targeted Gene Delivery. Chem Commun. 2010; 46:1851–1853.

53. Peng J, Garcia MA, Choi J-s, Zhao L, Chen K-J, Bernstein JR, Peyda P, Hsiao Y-S, Liu KW, Lin W-Y, Pyle AD, Wang H, Hou S, Tseng H-R. Molecular Recognition Enables Nanosubstrate-Mediated Delivery of Gene-Encapsulated Nanoparticles with High Efficiency. ACS Nano. 2014; 8:4621–4629. [PubMed: 24708312]

54. Hou S, Choi J-s, Chen K-J, Zhang Y, Peng J, Garcia MA, Yu J-H, Thakore-Shah K, Ro T, Chen J-F, Peyda P, Fan G, Pyle AD, Wang H, Tseng H-R. Supramolecular Nanosubstrate-Mediated Delivery for Reprogramming and Transdifferentiation of Mammalian Cells. Small. 2015; 11:2499–2504. [PubMed: 25613059]

55. Liu Y, Wang H, Kamei K, Yan M, Chen KJ, Yuan Q, Shi L, Lu Y, Tseng HR. Delivery of Intact Transcription Factor by Using Self-Assembled Supramolecular Nanoparticles. Angew Chem, Int Ed. 2011; 50:3058–3062.

56. Chen KJ, Tang L, Garcia MA, Wang H, Lu H, Lin WY, Hou S, Yin Q, Shen CK, Cheng J, Tseng HR. The Therapeutic Efficacy of Camptothecin-Encapsulated Supramolecular Nanoparticles. Biomaterials. 2012; 33:1162–1169. [PubMed: 22074663]

57. Boswell CA, Sun XK, Niu WJ, Weisman GR, Wong EH, Rheingold AL, Anderson CJ. Comparative *in Vivo* Stability of Copper-64-Labeled Cross-Bridged and Conventional Tetraazamacrocyclic Complexes. J Med Chem. 2004; 47:1465–1474. [PubMed: 14998334]

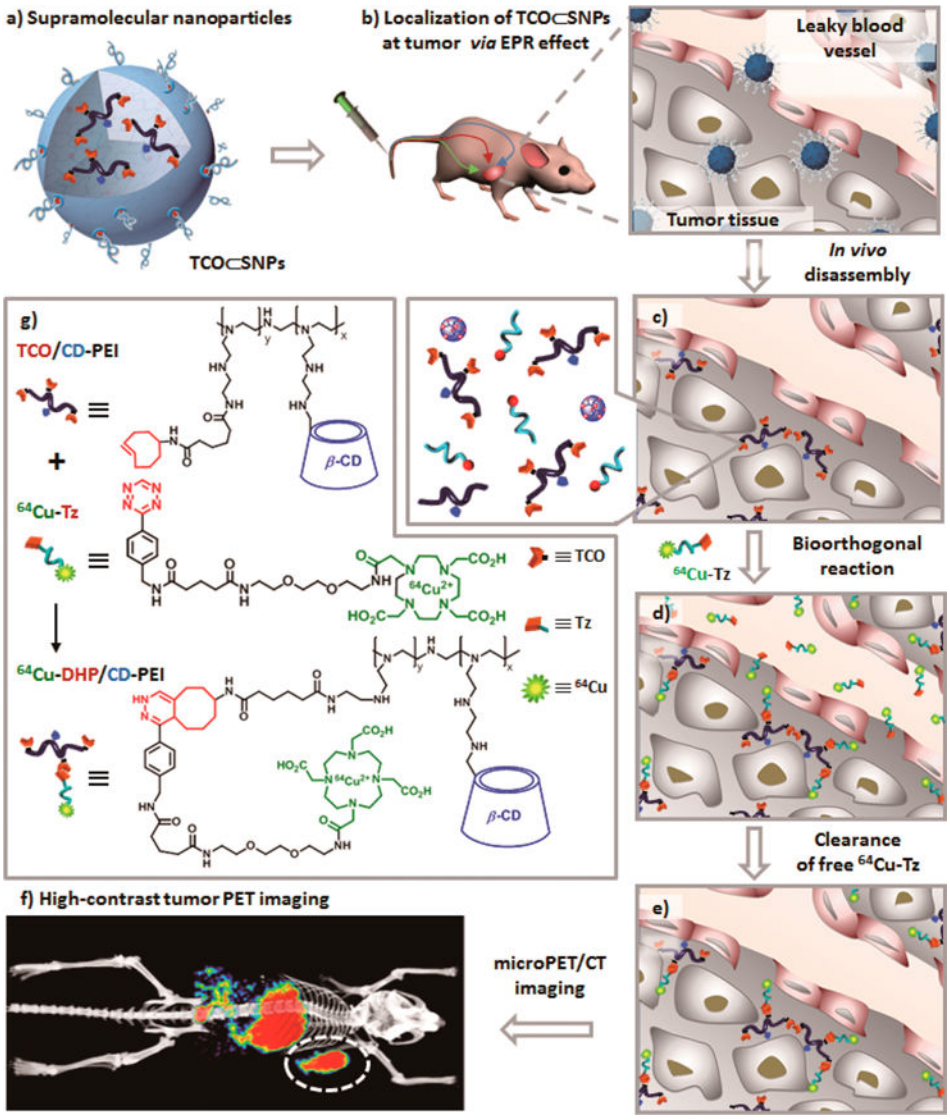

Figure 1.

Schematic representation of a new approach for pretargeted PET imaging that leverages the utilities of supramolecular nanoparticles (SNPs) and bioorthogonal chemistry: (a) Supramolecular synthetic strategy is employed for preparing the tumor-targeting agent (TCO⊂SNPs); (b) after intravenous injection, the tumor EPR effect drives preferential accumulation of TCO⊂SNPs in tumor; (c) after TCO⊂SNPs have accumulated in tumor, TCO⊂SNPs disassemble to release a TCO-grafted molecular building block, TCO/CD-PEI; (d) a radiolabeled reporter (^{64}Cu-Tz) is then injected for bioorthogonal reaction with tumor-retained TCO/CD-PEI; (e) the unreacted ^{64}Cu-Tz was cleared quickly from the body; (f) the resulting dihydropyrazine (DHP) conjugation adduct (^{64}Cu-DHP/CD-PEI) confines radioactivity in tumor, resulting in high-contrast tumor PET imaging. (g) Chemical structures of the bioorthogonal reactions between TCO/CD-PEI and ^{64}Cu-Tz.

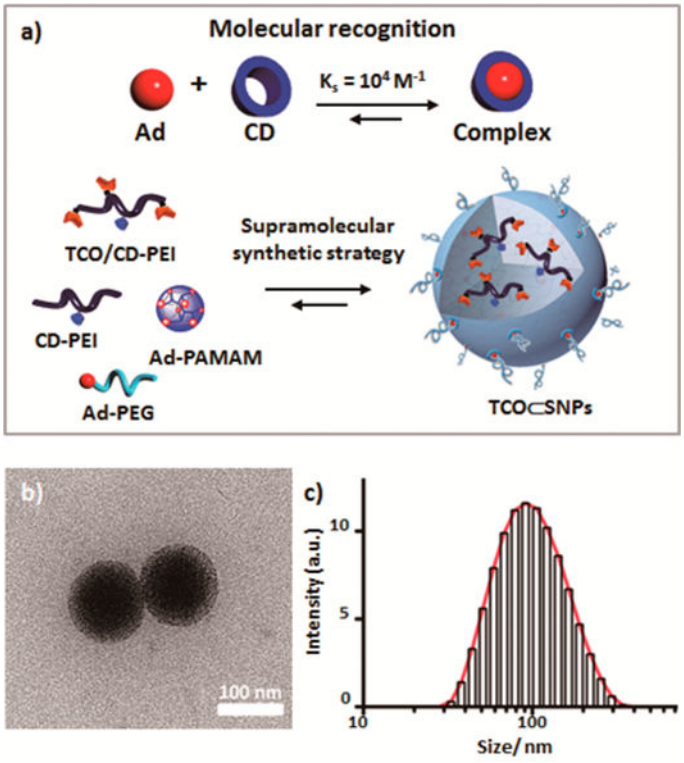

Figure 2.

(a) Schematic summary of the supramolecular synthetic strategy employed for preparation of the tumor-targeting agent (TCO⊂SNPs). (b) Transmission electron microscope image. (c) Dynamic light scattering measurement of TCO⊂SNPs.

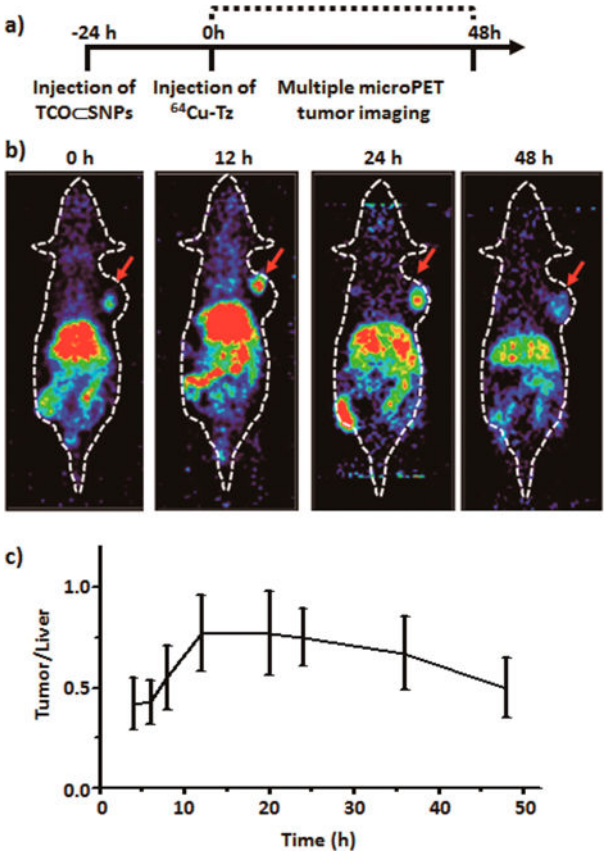

Figure 3.

(a) Timeline of the injection protocol employed for the pretargeted study. (b) MicroPET images of the pretargeted study at various time points. (c) Ratio of PET tumor signal to liver signal of xenografted mice from the preliminary pretargeted study ($n = 4$).

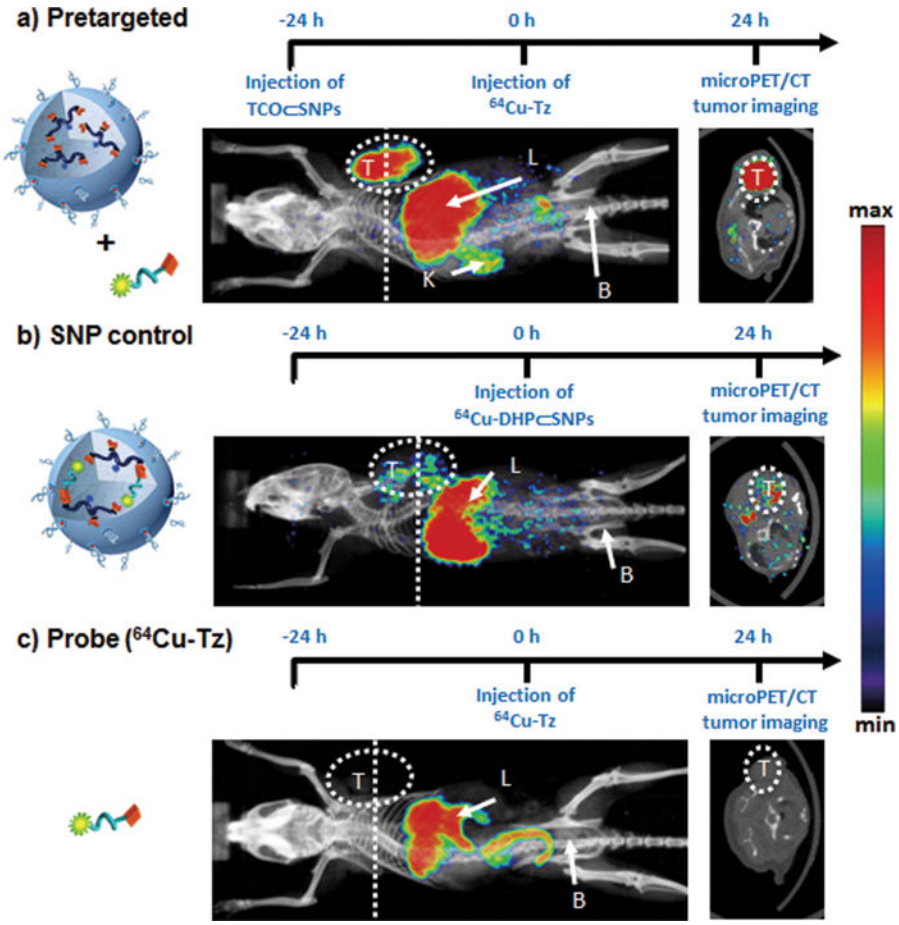

Figure 4.

Timeline of the injection protocol employed for (a) pretargeted, (b) SNP control (^{64}Cu-DHP⊂SNPs), and (c) free radiolabeled reporter (^{64}Cu-Tz) studies. Representative *in vivo* microPET/CT images of the mice (n = 4/group) subjected to the three studies at 24 h p.i. Labels T, L, K, and B refer to the tumor, liver, kidney, and bladder, respectively. Dashed lines correspond to the transverse cross-section through the center of each tumor mass, whose image is shown in the right panel.

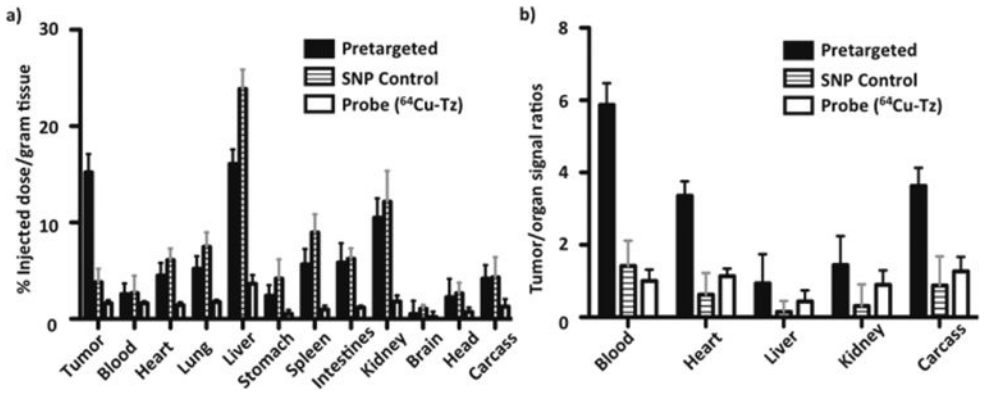

Figure 5.

(a) Quantitative *ex vivo* biodistribution data comparing radioactivity in various major organs among the pretargeted group, SNP control (^{64}Cu-DHP⊂SNPs) group, and radiolabeled reporter (^{64}Cu-Tz) alone group at the termination time point. (b) Ratios of tumor-to-organ signals in the three groups. Data are presented as mean ± standard deviation (n = 4).